# Large eddy simulation of ship airflow control with steady Coanda effect

(article starts on next page)

iD **Kewei Xu,** iD **Xinchao Su,** iD **Rickard Bensow, et al.**

**COLLECTIONS**

F    This paper was selected as Featured

View Online    Export Citation    CrossMark

---

**ARTICLES YOU MAY BE INTERESTED IN**

# Physics of Fluids

## Special Topic: Paint and Coating Physics

**Submit Today!**

**AIP Publishing**

# Large eddy simulation of ship airflow control with steady Coanda effect ⓕ

View Online    Export Citation    CrossMark

Kewei Xu,[a] ⓘ Xinchao Su, ⓘ Rickard Bensow, ⓘ and Sinisa Krajnovic[b] ⓘ

## AFFILIATIONS

Department of Mechanics and Maritime Sciences, Chalmers University of Technology, Gothenburg 412 96, Sweden

[a]Electronic mail: kewei@chalmers.se
[b]Author to whom correspondence should be addressed: sinisa.krajnovic@chalmers.se

## ABSTRACT

This paper numerically studies the steady Coanda effect for drag reduction and airwake manipulations on the Chalmers ship model (CSM) using large eddy simulation with wall-adapting local-eddy viscosity model. Numerical methods are validated by experimental data acquired from the baseline CSM. In creating the flow control model, the hanger base of the baseline CSM is modified with Coanda surfaces and injection slots along its roof edge and two side edges. Four representative cases are studied: a no-jet case and three cases with the same momentum coefficient of the jet flow activated at different locations (roof, sides, and combined). The results show that the four cases have various performances in drag reduction and vortex structures on the deck. They are also different in mean and turbulent quantities as well as POD (proper orthogonal decomposition) modes in their airwake. It is found that the roof-jet has a stronger Coanda effect and is more vectored toward the low-speed area (LSA) on the deck than the side-jets that detach earlier from the Coanda surface. The energization process is, therefore, different where the roof-jet is more effective that directly brings high momentum to LSA and side-jets manipulate shear layers for mixing enhancement. The cases with roof-jet achieve better mitigation of flow re-circulation and higher recovery of streamwise velocity with lower turbulent fluctuation in the airwake. POD analysis suggests that the roof-jet can stabilize the wake.

## I. INTRODUCTION

The studies of ship airwake began on the simple representative models, such as backward-facing step (BFS) or bluff bodies.[1] The flow features demonstrated using a rectangular bluff body[2] reveal the complex vortex structures in the wake with a dominated U-shaped vortex. Later, with extensive experimental efforts on the BFS,[3] the features of airwake are further understood, which includes shear layer separations, massive re-circulation region, and corner eddies (CE). Such flow features are finally evident on the deck of a ship model (DDG81),[4] confirming the qualitative similarities to those of BFS and rectangular bluff body. The main characteristics of the ship airwake explained by Shafer and Ghee[4] include severe flow separations, flow reattachment, and a horseshoe-shaped vortex with both ends contacting on the deck.

The ship airwake with complicated structures has a strong impact on the takeoff/landing environment for helicopter operations, which is, therefore, widely studied by many researchers.[5–11] Moreover, in the context of low emission, the reduction of fuel consumption for ship propulsion also draws growing attention. It is believed that the aforementioned two issues could be alleviated by a controlled ship airwake

with low unsteadiness, suppressed separation, and reduced size of a re-circulation region on the deck. In this regard, various flow control techniques are implemented and studied on ship models for airwake manipulation.

Categorizing these flow control techniques by the necessity of an external flow source, there are passive flow control (PFC) and active flow control (AFC) methods. For PFC methods, optimizing the hanger shape is straightforward to affect the downstream airwake. Bardera and Meseguer[12] modified the hanger roof of simple frigate shape (SFS) with different degrees of curvature. Experimental results indicated that the length of the shear layer was reduced to a maximum of 42% by the "C" shape model with the highest degree of curvature. Later, Bardera et al.[13] modified the hanger to a similar shape with the re-circulation bubble for an aerodynamically optimized geometry. The angled and elliptical hangers with roof and walls modified achieved the overall best performance considering the mitigation of unsteadiness, reduction of low-speed area (LSA), and loss of interior volume. Certain reduction of unsteadiness was achieved with even simpler adjustment. Shafer and Ghee[4] switched the surface material from solid to porous

of deck and hanger base, resulting in a reduction of unsteadiness up to 4.1%. Apart from the optimization of the hanger shape, passive flow control devices, such as vortex generators, lateral wedges, fences, and various types of aft ramps, were also studied. LaSalle[14] placed a notched fence on the top and the side of the hanger to modify ship airwake structures for more expansive helicopter flight envelopes. However, experimental and numerical results suggested that such a particular fence structure enhances the shear layer and turbulent fluctuation instead, which might bring marginal benefit for helicopter operations. Various PFC techniques, including flap, ramp, and notch, were studied on a ship model with high wind on deck (WOD) angles.[15] Substantial reductions of RMS (root mean square) forces and moments on helicopters were achieved by side-flap and notch. Similar studies were also conducted by Yongjie et al.[16] who implemented ramp and notch on hanger roof and remarkably reduced the RMS rotor loading.

For active flow control methods, external flow sources were required to produce high-energy jet flow. The steady blowing jet studied by Shafer and Ghee[4] was found effective to mitigate the unsteadiness in the landing region. With an injection velocity of 2.5% of the free-stream, the unsteadiness was reduced by 6.6% in a headwind, and such improvement was more significant with high WOD. In the study by Gallas et al.[9] on a simplified frigate ONERA (SFO) model, the steady blowing jet was perpendicularly ejected through the slots along the roof and sides of the hanger base. It was found that the re-circulation zone (RZ) was suppressed due to the enhanced mixing activities and entrainment by the jet. Other than the blowing jet, the steady suction was also studied for ship airwake control. Bardera et al.[17] tested various suction configurations on the ship deck and conducted parametric studies of suction power and suction holes. The configuration with the highest flow rate and hole diameter could effectively reduce the low-speed zone from 36% to 3%. The control authorities of injection and suction were compared by Matías-García et al.[18] who found that the injection reduces the low-speed region twice as much as the suction does.

The previous flow control studies of ship airwake mainly focus on the mitigation of unsteadiness, suppression of low-speed area on the deck, and improvement of helicopter operations. However, little attention has been paid to the reduction of ship aerodynamic drag, which is significant to achieve lower power consumption and emission. Moreover, the previous AFC study[9] ejects the jet perpendicularly to the hanger base with the jet flow parallel with the main-flow. Comparatively, a vectored jet heading toward the low-speed area or the re-circulation region could be more efficient for energization. The Coanda effect[19] is one possible approach to achieve such modification of the jet. It has been widely used in active flow control,[20–22] especially for improving the aerodynamic performance of a ship,[23] bluff bodies,[24–28] ground vehicles,[29,30] and airfoils.[31–34] Furthermore, although the mixing process enhanced by the steady blowing jet[9] benefits the suppression of the re-circulation zone, it also increases the downstream turbulent intensity, which may deteriorate the environment for helicopter operation. Therefore, an injection method that achieves effective re-circulation mitigation, as well as reduced turbulent activities would be more desirable.

This paper applies the steady Coanda effect on the Chalmers ship model (CSM) for drag reduction and airwake manipulations. The numerical method of large eddy simulation (LES) is validated using experimental data acquired on the baseline CSM without flow control. The Coanda surfaces and injection slots are implemented along the three edges of the hanger base, namely, the roof, left, and right sides. Four cases are studied with the same jet momentum coefficients blown from different slots: the no-jet case 1, case 2 with the jet blown from the roof and sides slots, case 3 with the jet blown only from the roof slot, and case 4 with the jet blown only from the sides slots. This is to study the effects of jet locations on the base pressure recovery for drag reduction and on airwake manipulations in terms of streamwise flow, down-wash flow, and turbulent fluctuations. Although the steady blowing jet has been studied previously on a ship model, it was not combined with Coanda effects. The objective of this paper is to achieve a more desired control effectiveness of the ship airwake and bring further understanding of the control mechanism in the new context.

## II. SHIP MODEL AND EXPERIMENTAL SETUP

The baseline Chalmers ship model (CSM) as shown in the top of Fig. 1 used in the present study consists of a bow, hanger, base, deck, and stern. The width to height ratio ($W/h$) of the hanger is 0.45 and is similar to that of the simplified ship model [SFS2 (Ref. 12)]. The details of model dimensions are shown in the middle and bottom of Fig. 1. The width of the hanger is used as the characteristic length for normalization.

The baseline CSM has a square-back shape of the base as shown in Fig. 1. The flow control model shown in Fig. 2 is modified based on the baseline CSM, which adds the injection slots near all edges (two sides and roof) of the base and modifies the square-back to a quarter-ellipse-shaped Coanda surface. The ellipse shape is kept the same
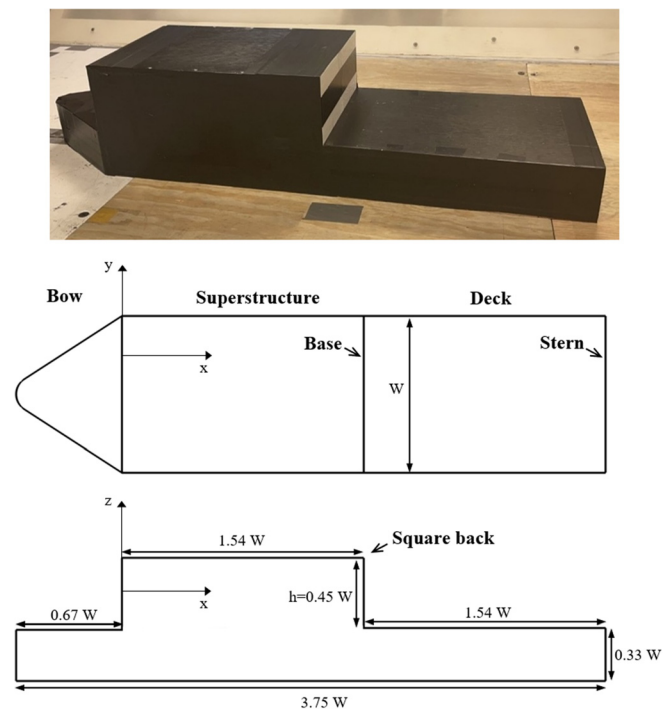


**FIG. 1.** The Chalmers ship model (top) and its dimensions in plan (middle) and side (bottom) views.
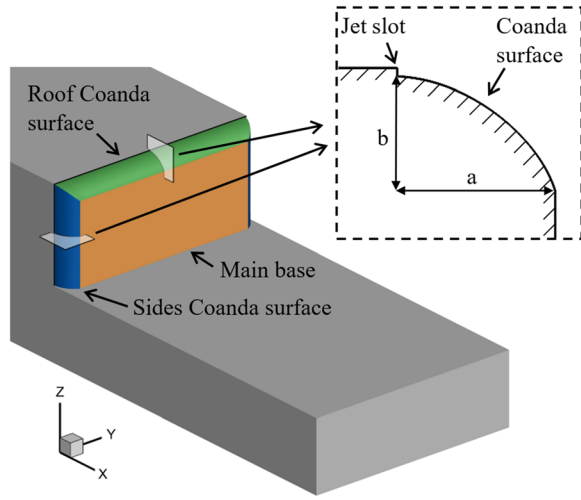
**FIG. 2.** Modification of Coanda surfaces and jet slots.

among sides and roof with a semi-major axis ($a$) of 20%$h$ and a semi-minor axis ($b$) of 15%$h$, where $h$ is the hanger height. The modified ship base, therefore, consists of three regions as shown in Fig. 2: the roof Coanda surface (green), the sides Coanda surfaces (blue), and the main base (orange). Modifying the square-back to ellipse shape causes a volume loss of hanger by 0.4%.

The experimental study is conducted on the baseline CSM to acquire the drag force and pressure distributions for numerical validations. The testing of the flow control model is not included in the present paper. The experiments are conducted in the closed-circuit L2 wind tunnel facilities with a test section of $1.8 \times 1.25 \times 3$ m$^3$ (Fig. 3). The wind tunnel has the speed range of 0–60 m/s, and the baseline CSM is tested at $U_\infty = 5$ m/s, which yields a Reynolds number ($Re$) of $8 \times 10^4$ based on the ship width. As illustrated in Fig. 3(a), the ship model is mounted on a six-component strain-gauge balance from RUAG of type 196–6H that is positioned underneath the tunnel floor. The drag force ($F_D$) acquired by the force balance is an averaged value
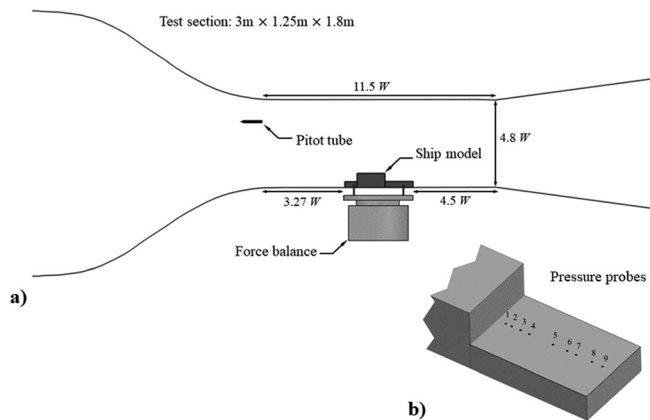


**FIG. 3.** Schematics of Chalmers L2 wind tunnel and the locations of the pressure probes.

**TABLE I.** Locations of the pressure probes ($x/W$).

| Numbers | 1 | 2 | 3 | 4 | 5 | 6 | 7 | 8 | 9 |
|---|---|---|---|---|---|---|---|---|---|
| Locations | 0.08 | 0.14 | 0.24 | 0.54 | 0.73 | 0.92 | 1.10 | 1.25 | 1.38 |

for 20 s. The drag coefficient ($C_D$) is the normalization of $F_D$ using Eq. (1) with free-stream values

$$C_D = \frac{F_D}{0.5\rho_\infty U_\infty^2 A_s}, \tag{1}$$

where $\rho_\infty$ and $U_\infty$ are the free-stream density and velocity, and $A_s$ is the ship cross-sectional area.

The pressure measurements are conducted using the differential pressure scanner 9116 with a scanning frequency of 62.5 Hz and a sampling time of 120 s. The pressure distribution is obtained by the pressure probes that are located along the center of the deck as shown in Fig. 3(b). Table I presents the specific positions of probes relative to the base.

The pressure coefficient is obtained based on the measured pressure using the following equation:

$$C_p = \frac{p - p_\infty}{0.5\rho_\infty U_\infty^2}, \tag{2}$$

where $p$ is the measured pressure on the deck, and $p_\infty$, $\rho_\infty$, and $U_\infty$ are the free-stream pressure, density, and velocity, respectively.

## III. NUMERICAL METHODS AND VALIDATIONS

Large eddy simulation (LES) is conducted using the commercial finite volume software, Star-CCM+. The governing equations are the incompressible, spatially filtered 3D Navier–Stokes equations, which keep the unsteadiness associated with the large-scale turbulent motion and model the small-scale high-frequency components of the fluid motion. The filter width, $\Delta$, is associated with the cell size and is defined as $\Delta = (\Delta_i \Delta_j \Delta_k)^{1/3}$. The wall-adapting local-eddy viscosity (WALE) model proposed by Nicoud and Ducros[35] is employed in the present study to provide the subgrid-scale viscosity ($\mu_t$) in the Boussinesq approximation of the subgrid-scale stress tensor. The WALE model has been extensively validated on predicting flows around the hatch back,[36] the square back,[37] and the notch back[38,39] Ahmed bodies. The WALE model computes the subgrid eddy viscosity based on the invariants of the velocity gradient and accounts for the rotational rate. It is defined as

$$\mu_t = \rho (C_w \Delta)^2 \frac{(S_{ij}^* S_{ij}^*)^{3/2}}{(\tilde{S}_{ij} \tilde{S}_{ij})^{5/2} + (S_{ij}^* S_{ij}^*)^{5/4}}, \tag{3}$$

where the model coefficient $C_w$ is 0.544. $\tilde{S}$ is the strain rate tensor that is computed from the resolved velocity field. $S_{ij}^*$ is the traceless symmetric part of the square of the velocity gradient tensor, defined as

$$S_{ij}^* = \frac{1}{2}(\tilde{g}_{ij}^2 + \tilde{g}_{ji}^2) - \frac{1}{3}\delta_{ij}\tilde{g}_{kk}^2, \tag{4}$$

where $\delta_{ij}$ is the Kronecker delta, and $g_{ij} = \partial u_i / \partial x_j$.

The convective flux is evaluated by a bounded central-differencing scheme that blends 98% of the second-order central-
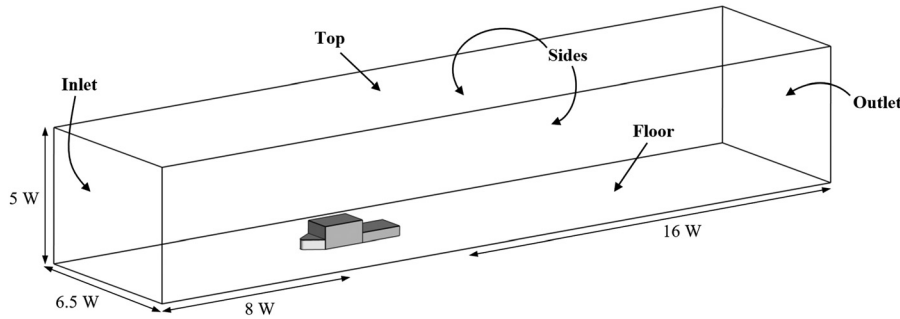
**FIG. 4.** Computational domain.

differencing scheme and 2% of the first-order upwind scheme for robustness purpose. The implicit unsteady solver with second-order Euler implicit scheme is used to approximate the transient term. The physical time step ($\Delta t$) is set to $1.44 \times 10^{-4}$ s, which ensures that the CFL (Courant–Friedrichs–Lewy) number is lower than 1 in over 99% of the cells. LES simulation starts from a preliminary flow field that is provided by a Unsteady Reynolds-averaged Navier–Stokes (URANS) simulation with the $k - \omega$ shear stress transport (SST) turbulence model. After a characteristic time ($t^* = tU_\infty/h$) of 65, when all the aerodynamic forces become dynamically stable, LES simulation begins sampling and averaging results for a $t^*$ of 130. The present LES simulation is conducted using Tetralith general computing resource provided by SNIC (Swedish National Infrastructure for Computing) at the National Supercomputer Center (NSC). Each case in the present study requires about 41 472 CPU hours and 384 cores (Intel Xeon Gold 6130 processors).

Figure 4 shows the computational domain with a cross-sectional area of $6.5\,W \times 5W$, which accounts for a blockage ratio of about 2.4%. The length of the domain is $28W$ with $8W$ from the inlet to the bow tip-point and $16W$ from the stern to the outlet. The ship model sits on the floor with no gap in-between. The coordinates system and the velocity direction are denoted by $x$ and $u$ in the streamwise direction, $y$ and $v$ in the spanwise direction, and $z$ and $w$ in the vertical direction. The velocity inflow boundary condition with a uniform free-stream velocity $U_\infty = 5$ m/s is specified at the inlet. Static pressure outlet boundary condition is applied at the outlet. The top and sides of the domain are specified with the symmetry boundary condition. The no-

slip wall boundary condition is applied on the floor and all ship surfaces. For the cases with flow control, velocity inlet boundary condition is specified at the injection exit without injection duct simulated.

The structured hexahedral mesh is created using Pointwise. Figure 5 shows the details of the mesh topology, where the top-right figure is a cross-sectional slide, and the bottom-right figure is the top view at the ship bow. The initial mesh size contains $37 \times 10^6$ cells for the baseline model and $42 \times 10^6$ cells for the model with flow control. Based on various numerical studies[40–42] on ships with the grid size ranging from 6 to $21 \times 10^6$ cells, a grid size of $37 \times 10^6$ cells for the present study is expected to be sufficient. The near-wall grid distance $\Delta y$ is $3 \times 10^{-5}$, which ensures $y^+ = \frac{\Delta y u_\tau}{\nu}$ lower than 1. For the resolution in the streamwise ($\Delta s^+ = \frac{\Delta s u_\tau}{\nu}$) and spanwise ($\Delta l^+ = \frac{\Delta l u_\tau}{\nu}$) directions, $\Delta s^+$ is less than 55, and the maximum $\Delta l^+$ is 21, which satisfies the suggested ranges proposed by Piomelli and Chasnov.[43] Furthermore, as shown in Table II, a grid independent study is conducted based on a coarse mesh of $27 \times 10^6$ cells and a fine mesh of $47 \times 10^6$ cells. The acquired drag coefficients ($C_D$) fall in a very close range with the deviation ($\Delta C_D$) from the initial mesh by less than 0.9%. It also shows that $C_D$ acquired by the initial mesh is more consistent with the fine mesh, which suggests the convergence of solutions to the fine mesh. Note that the predicted drag force is acquired by integrating the surface pressure and wall shear stress in the $x$ (free-stream) direction.

The numerical method is validated by comparing the drag force and $C_p$ distribution with the experimental measurements. The initial mesh predicts $C_D$ of 0.562 as shown in Table II and is 4.2% deviated from the experimental value of 0.587.

Then, the $C_p$ distribution along the center of the deck [Fig. 3(b)] is used for further validation. Figure 6 shows the predicted and experimental $C_p$ distributions are in good agreement from the base ($x/W = 0$) to deck-end ($x/W = 1.54$). The deck pressure first decreases to the minimum due to the re-circulation bubble, and then, the flow reattachment on the deck increases pressure to the peak value. The maximum discrepancy of $C_p$ distributions locates at the deep separation of
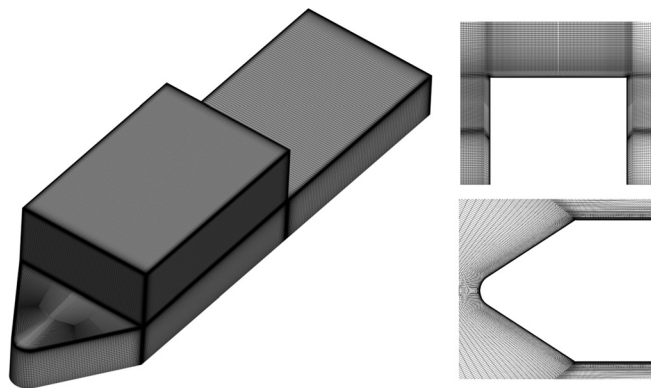


**FIG. 5.** Mesh topology of the Chalmers ship model.

**TABLE II.** Results of the grid independent study.

| Cases | $y_{max}^+$ | $\Delta s_{max}^+$ | $\Delta l_{max}^+$ | No. of cells | $C_D$ | $\Delta C_D$ |
|---|---|---|---|---|---|---|
| Initial | <1 | <55 | <21 | $3.7 \times 10^7$ | 0.562 | $\cdots$ |
| Coarse | <1 | <65 | <30 | $2.6 \times 10^7$ | 0.567 | 0.88% |
| Fine | <1 | <40 | <15 | $4.7 \times 10^7$ | 0.564 | 0.35% |
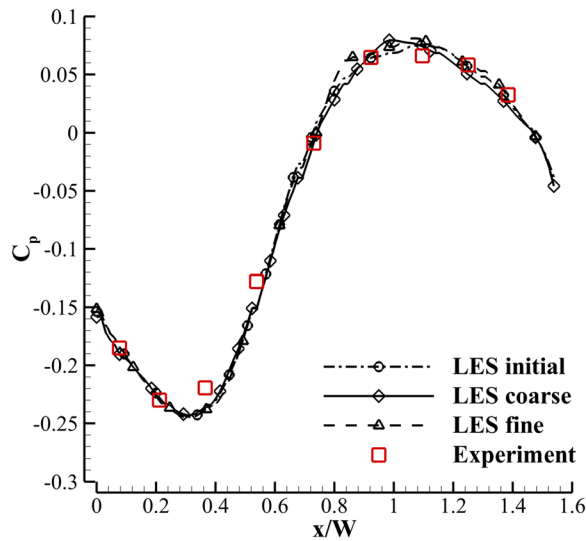
**FIG. 6.** $C_p$ distributions at the center of the deck.

**TABLE III.** Drag reduction among cases.

| Cases | $C_\mu$ | $C_d$ | $\Delta C_d$ |
|---|---|---|---|
| Baseline | $\cdots$ | 0.562 | $\cdots$ |
| Case 1 | 0 | 0.561 | 0.2% |
| Case 2 | 0.02 | 0.520 | 7.5% |
| Case 3 | 0.02 | 0.558 | 0.7% |
| Case 4 | 0.02 | 0.533 | 5.2% |

$x/W = 0.38$, which is usually challenging in flow predictions. Similar discrepancy at such location are also reported in other ship research.[40,42] Figure 6 also shows that the predicted $C_p$ distributions acquired by the three meshes are virtually overlapped, further supporting the grid independence. Overall, it is indicated that the current numerical method is capable to predict the flow around the CSM with a satisfied accuracy, and the grid independence is achieved with the initial mesh size of $37 \times 10^6$ cells.

## IV. RESULTS AND DISCUSSION

This section presents the results of the CSM with the steady Coanda effect applied at different locations of the base. Discussions focus on drag reduction, airwake manipulation, flow control, and energy transfer mechanism. Four cases are investigated, labeled as case 1–4: (1) the modified base configuration with Coanda surface but no-jet blowing, (2) blowing from the roof as well as from both sides, (3) blowing from the roof slot only, and (4) blowing from the sides slots only. The three flow control cases 2–4 are kept with the same jet momentum coefficient ($C_\mu$) of 0.02, where case 2 distributes $C_\mu$ of 0.0125 from roof blowing and 0.0075 from sides, which results in a roof $U_j$ of $1.1 \times U_\infty$ and sides $U_j$ of $0.9 \times U_\infty$. Since cases 3 and 4 only inject jets from either roof or side slots, their injection velocity is higher than that of case 2 to maintain the same $C_\mu$, corresponding to a $U_j$ of about $1.4 \times U_\infty$. Since the $U_j$ in cases 3 and 4 are similar, the performance difference between these cases can be, therefore, attributed to the locations where the jet is applied. The jet momentum coefficient $C_\mu$ is defined as

$$C_\mu = \frac{\dot{m}_j U_j}{0.5 \rho_\infty U_\infty^2 A_s},\tag{5}$$

where $\dot{m}_j$ and $U_j$ are the mass flow rate and the velocity of the jet, respectively.

## A. Control effectiveness and flow structures

Table III compares the drag coefficients of the four cases and their drag reduction in percentage. Without jet blowing, case 1 achieves a minor drag reduction of 0.2% compared to the baseline case. This suggests that the modified Coanda surface does not bring much drag reduction. With jet blowing, cases 2 and 4 reduce drag by 7.5% and 5.2%, whereas case 3 achieves only a minor drag reduction of 0.7%.

Figure 7 shows the time-averaged static pressure contours at the hanger base and stern of the four cases. Gauge pressure is used here with a unit of (Pa). Among the four cases, a notable pressure difference is observed at the base, whereas the stern pressure is varied slightly. Compared with case 1, the base pressure recovery is observed in all jet blowing cases 2–4. Case 2 with top and sides blowing achieves a significant pressure recovery near both sides and center regions of the main base as shown in Fig. 7(b). Case 3 with a stronger roof-jet further enlarges the high-pressure region at the bottom of the main base. However, penalties come with the roof blowing as indicated by the reduced pressure on the roof Coanda surface in cases 2 and 3, which offsets the achieved base pressure recovery. This is because the high-velocity jet attaching on the curved Coanda surface reduces the local pressure. Such a pressure-decreasing effect is enhanced in case 3 due to a higher roof-jet velocity, which is why case 3 yields a minor drag reduction in Table III. Reduced pressure recovery is achieved in case 4 with side-jets only as shown in Fig. 7(d). However, without pressure reduction at the roof Coanda surface, case 4 achieves a higher drag reduction than case 3.

To demonstrate jet effects on suppressing the re-circulation bubble, Fig. 8 shows the $u$ contours from the side-view at the symmetric plane. A low-speed area (LSA) on the deck is highlighted by the white iso-line with $u = 0$ m/s. Compared with case 1, the LSA downstream the hanger base is substantially reduced in case 2 due to the well-attached roof-jet as shown in the zoomed-in view in Fig. 8(b). As the velocity of the roof-jet increased in case 3, the Coanda effect is enhanced with a better attachment of jet that further suppresses the LSA as shown in Fig. 8(c). Comparatively, the sides blowing case 4 does not present a significant effect on LSA mitigation. Figure 9 shows the $u$ contours from the top-view in the z-plane at the mid-base height. Similarly, the LSA enclosed by the iso-line with $u = 0$ is colored in white. A bell-shaped LSA is observed in the no-jet case 1. Due to the energization from the roof-jet, the LSA of cases 2 and 3 is reduced in the center region, especially in case 3, where the LSA is eliminated in the center. Such LSA reduction is weakened toward the sides because of the flow re-circulation at sides. In case 4, the LSA is constrained toward the center, but its size is not much reduced as compared to case 1. The side-jets as shown in the zoomed-view in Figs. 9(b) and 9(d)
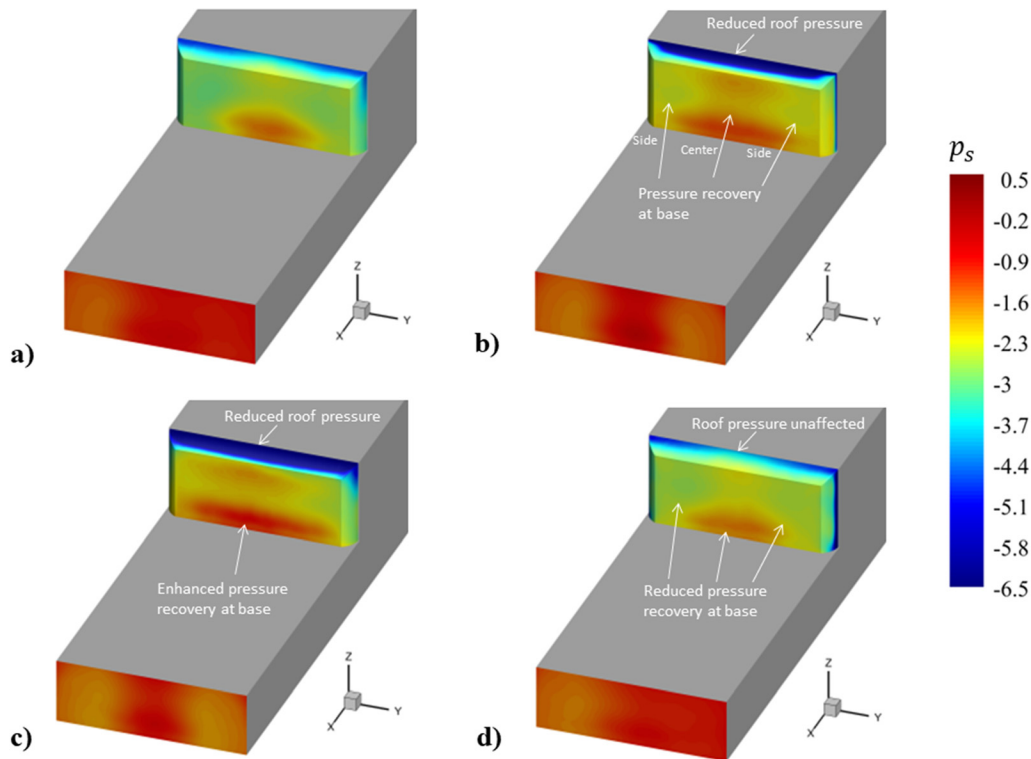
**FIG. 7.** Time-averaged static pressure ($p_s$) contours at the base and the stern: (a) case 1, (b) case 2, (c) case 3, and (d) case 4.

detach earlier than the roof-jet shown in Figs. 8(b) and 8(d), which fail to guide the high-energy flow toward the LSA for energization. Therefore, side-jets are less effective to achieve bubble suppression and pressure recovery.

A question of interest is why the roof-jet attach better than side-jets, even in case 3 and 4 where $C_\mu$ is the same between the sides and roof jets. This can be explained by the surface pressure difference between the roof and sides Coanda surface. As shown in Fig. 7(a) of the no-jet blowing case, the static pressure of the roof Coanda surface is much lower than that of the side Coanda surfaces. The low surface pressure enhances the pressure gradient pointing from the ambient to

the surface. As the jet is blown from slots, the higher pressure gradient pushes the jet to stay on the roof Coanda surface, and therefore, a better attachment is achieved. Moreover, the attached jet accelerating on the roof Coanda surface will further reduce the surface pressure, which again benefits the jet attachment.

Figure 10 shows the flow structures of the four cases using streamlines in the symmetric plane and the z-plane, and the distributions of the vortex core are marked by the blue lines. The left-top figure is the front view of the vortex core. The re-circulation zone is shown by the iso-surface of streamwise velocity $u = 0$. A horseshoe-shaped vortex structure is observed right downstream the base in case 1 [Fig. 10(a)],
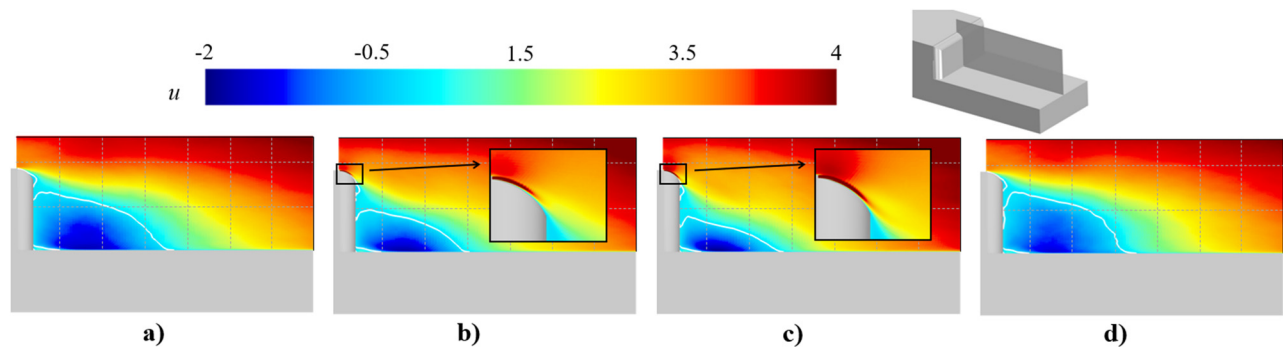


**FIG. 8.** Time-averaged $u$ contours at the symmetric plane with LSA marked by the white iso-line of $u = 0$: (a) case 1, (b) case 2, (c) case 3, and (d) case 4.
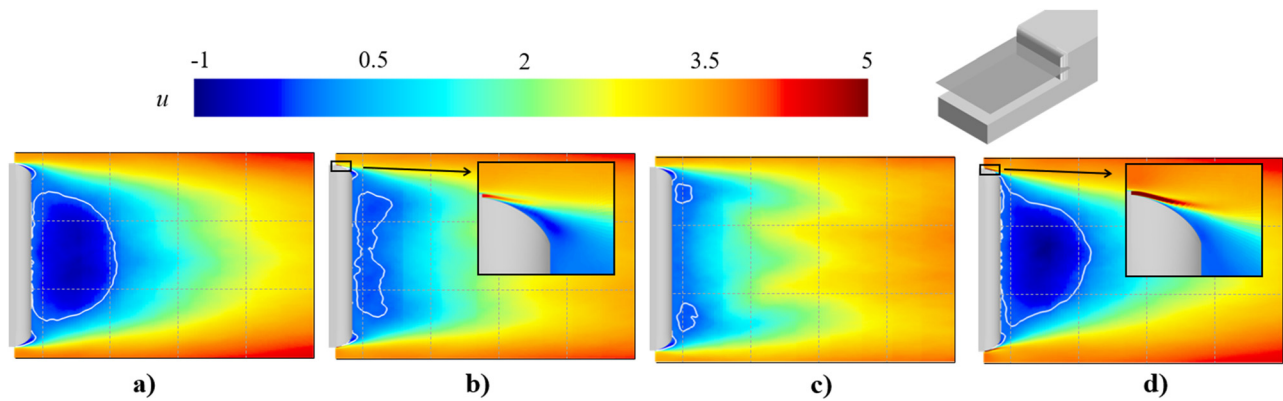
**FIG. 9.** Time-averaged $u$ contours at the z-plane with LSA marked by the white iso-line of $u = 0$: (a) case 1, (b) case 2, (c) case 3, and (d) case 4.

which is a typical structure observed on the flight deck of ships.[4] The upstream flow separates at the roof trailing edge causing the flow to re-circulate behind the base shown by the RZ (re-circulation zone) in Fig. 10. Resulting from the flow re-circulation, CEs (corner eddies), also reported by Driver *et al.*,[3] are formed along the bottom edge of the base in all cases. Additionally, the flow also separates at the both sides of the ship inducing a CV (counter-rotational vortex) at each side of the base, which contributes to the formation of the horseshoe shape. The vortex

structure varies among the four cases due to the jet injected from different locations, roof or sides. To quantify such size variation, Table IV presents the width ($w_{vc}$) and the center height ($h_{vc}$) of the vortex structure, where the ship width ($W$) is used for normalization. $\Delta h_{vc}$ and $\Delta w_{vc}$ denote the change in the height and width with respective to those of case 1 without jet. As shown in the front view on the left-top of Fig. 10(a), the vortex structure has a convex shape in the center with a $h_{vc}$ of 0.273 and $w_{vc}$ of 0.750. In case 2, the $h_{vc}$ is reduced by 29.6%
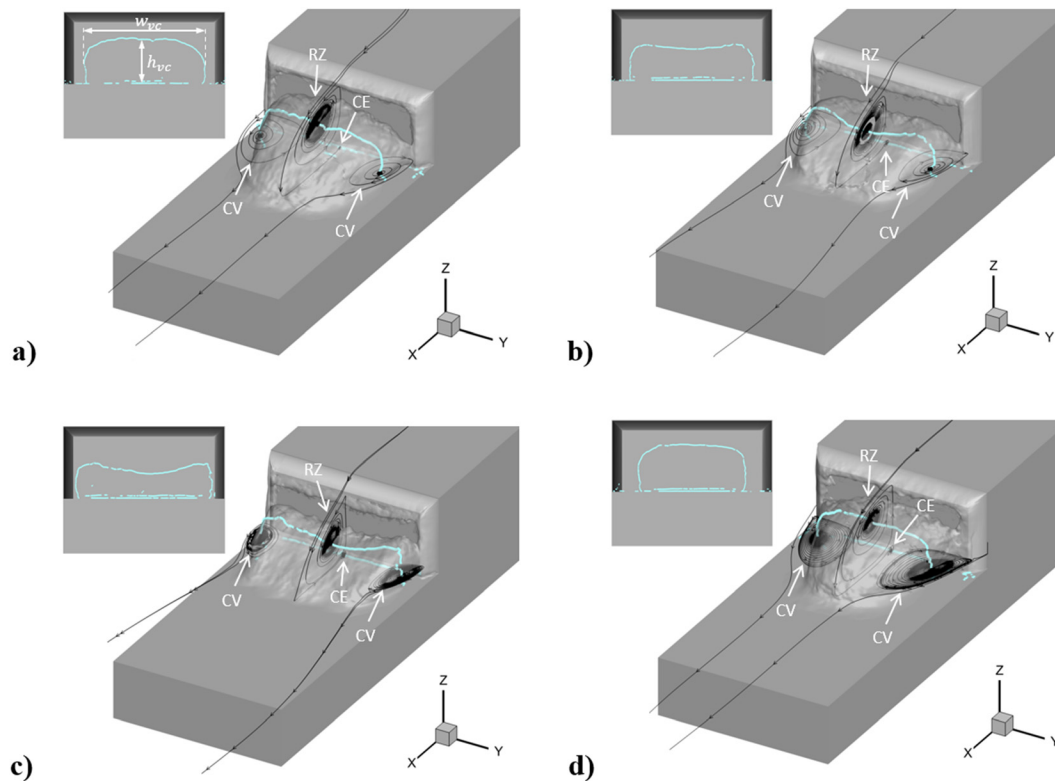


**FIG. 10.** Flow structures on the deck with the vortex core colored in blue, iso-surface with the time-averaged $u = 0$, and streamlines: (a) case 1, (b) case 2, (c) case 3, and (d) case 4.

**TABLE IV.** Variation in the vortex core size in width and height.

| Cases | $h_{vc}$ | $\Delta h_{vc}$ | $w_{vc}$ | $\Delta w_{vc}$ |
|---|---|---|---|---|
| Case 1 | 0.273 | $\cdots$ | 0.195 | $\cdots$ |
| Case 2 | 0.192 | $-29.6\%$ | 0.199 | $2.05\%$ |
| Case 3 | 0.154 | $-43.6\%$ | 0.219 | $12.3\%$ |
| Case 4 | 0.296 | $8.45\%$ | 0.172 | $-11.8\%$ |

associated with a slight increase in $w_{vc}$ of 2.05%. The convex shape of the vortex core becomes flat, and the re-circulation zone is squeezed toward the deck due to the energization of the roof-jet. With a stronger roof-jet in case 3, a concave shape at the center of the vortex core is manifested with $h_{vc}$ reduced by 43.6%, and the re-circulation zone is further squashed toward the deck. As a result, $w_{vc}$ is increased by 12.3%, and counter-rotational vortexes together with their wake flow are pushed to the sides. In case 4 with side-jets only, the vortex core maintains the same convex shape as case 1 but is constrained toward the center of the deck by the high-energy side-jets, and $w_{vc}$ is reduced by 11.8%. The center region of the re-circulation zone is, therefore, elevated with $h_{vc}$ increased by 8.45%. The wake flow from the side vortexes is also guided toward the center of the deck.

The time-averaged y-vorticity ($\omega_y$, spanwise) contours at the symmetric plane are shown in Fig. 11 to demonstrate the energy transfer process in the vertical direction by the roof-jet. The vorticity is presented with a unit of $(s^{-1})$. To facilitate the comparison, angle $\alpha$ is defined between the y-vorticity sheet to horizontal. The larger the $\alpha$, the closer the y-vorticity gets to the LSA, meaning the energization occurred where it is more needed. Case 1 only with the Coanda surface modified has the $\alpha$ angle of 15°, and the vorticity sheet is positioned high above the deck, away from the LSA. As the roof-jet starts to play a role in case 2, the vorticity sheet is vectored toward LSA with the $\alpha$ angle increased to 30°. As the roof-jet becomes stronger in case 3, the vorticity sheet is further vectored with an $\alpha = 45°$ due to enhanced Coanda effects. The vorticity sheet penetrates through the LSA for an effective energization process. Case 4 has the reduced $\alpha$ angle as compared to case 1 due to the elevated bubble by side-jets. Figure 12 shows the spanwise y-vorticity behavior using the iso-surface of $\omega_y = 70$. Minor vectoring effects of the vorticity sheet are observed in cases 1 and 4, whereas cases 2 and 3 maintain the strongly vectored vorticity sheet along the span.

Since side-jets mainly affect the z-vorticity ($\omega_z$, vertical), Fig. 13 shows the time-averaged z-vorticity contours on the z-plane at the mid-base height location. Similar to $\alpha$, $\beta$ angle is defined here to quantify the angle of z-vorticity sheet. Overall, the side-jets do not guide the vorticity sheet as much as the roof-jet since the $\beta$ angle enhancement is substantially lower than the $\alpha$ angle. The $\beta$ angles in non-sides-blowing cases 1 and 3 are 10° and 8°, respectively. With side-jets activated in case 2, the $\beta$ angle is merely increased by 4°. Further increasing of the side-jets' intensity in case 4 results in 2° increment. The iso-surface of $\omega_z = \pm 90$ is shown in Fig. 14 to illustrate the z-vorticity behavior along the vertical direction. With the side-jets activated in cases 2 and 4, vorticity sheets are more condensed than in cases 1 and 3, but no significant vectoring effect is observed. The less vectored z-vorticity sheet indicates that the energy transfer fails to be guided toward the LSA, which is inefficient. Overall, the jet blown from the sides has an inferior control authority compared to the roof-jet and, thus, has reduced effectiveness in bubble suppression and base pressure recovery.

## B. Effects on the airwake manipulations

This section is to demonstrate how the ship airwake is affected by the steady Coanda effects in terms of the mean quantities and fluctuating turbulent intensity. The flow fields on the ship deck are studied at four streamwise stations with $x/W$ of 0.3, 0.7, 1.1, and 1.5, where $W$ is the width of the deck, and $x/W = 0$ is the location of the hanger base.

One of the important mean quantities is the streamwise velocity $u$ on the ship deck. A higher incoming $u$ velocity enables the helicopter to takeoff at a higher gross weight.[4] Figure 15 shows the time-averaged $u$ contours at the four stations of interest. A low-speed region is observed at station 1 in all cases, where cases 2 and 3 with roof-jet have a significantly reduced size. The side-jets in case 4 mainly constrain the low-speed region to the center of the deck. Comparing case 3 with case 4, the roof-jet recovers higher velocity for the airwake as shown in the downstream stations 2, 3, and 4. This is because the roof-jet has a stronger induction effect due to the fine attachment on the Coanda surface, which guides the main-flow toward the deck for increasing $u$ velocity. Specifically, since the effect of the roof-jet is stronger in the center while dissipating toward the sides, the downstream stations 3 and 4 in cases 2 and 3 are recovered with higher $u$ velocity in the center region than the side region.
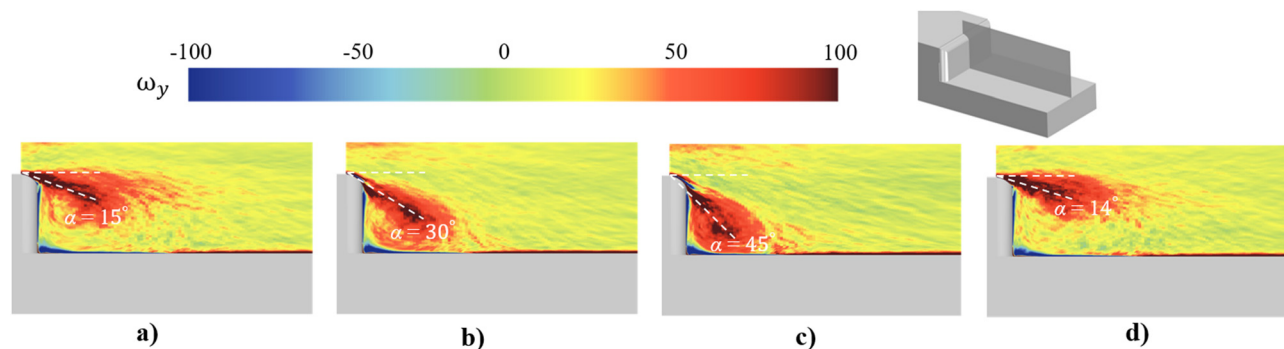


**FIG. 11.** Time-averaged y-vorticity at the symmetric plane: (a) case 1, (b) case 2, (c) case 3, and (d) case 4.
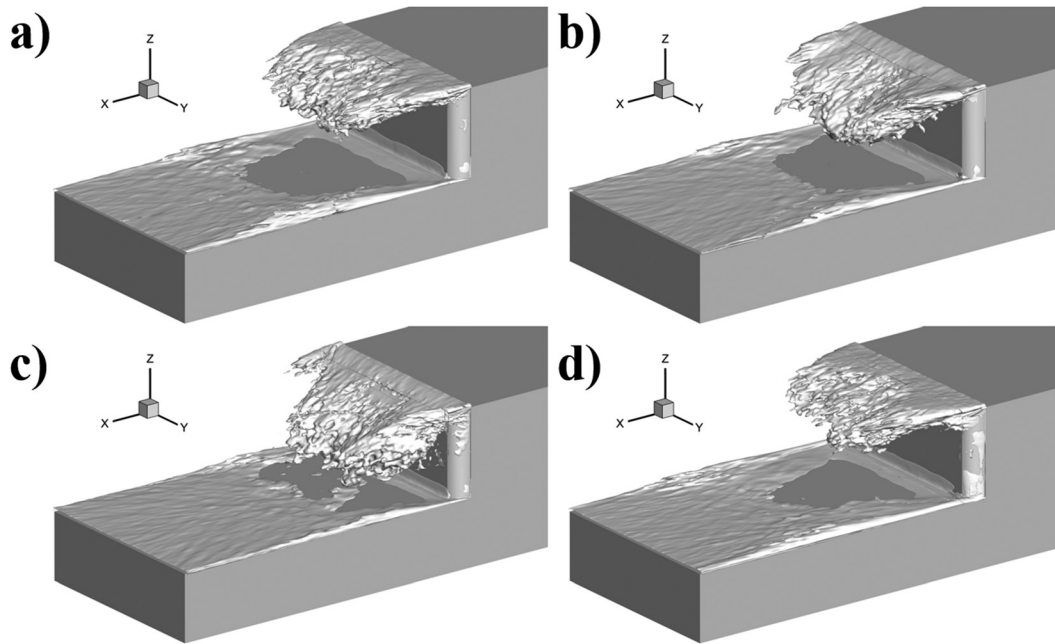
**FIG. 12.** Iso-surface of the time-averaged y-vorticity $= 70$: (a) case 1, (b) case 2, (c) case 3, and (d) case 4.

However, the strong induction effect from the roof-jet comes with a side-effect that enhances the down-wash flow, leading to potential safety issues for helicopter operation. Figure 16 shows the time-averaged $w$ (vertical direction) contours for the four cases, where a negative $w$ velocity indicates the down-wash flow. A minor down-wash region is observed in case 1 at stations 1 and 2. Comparatively, cases 2 and 3 have intensified negative-$w$ zones due to the vectored roof-jet and the enhanced induction of the main-flow. A mitigated negative-$w$ zone is observed in case 4 with side-jets only. This is because the side-jets elevate the re-circulation bubble downstream the base as shown in Fig. 10, which blocks the potential flow path for down washing.

To investigate the effects of flow control on wake dynamics, the proper orthogonal decomposition (POD) of the velocity field is conducted at the mid-base-height z-plane. The data sampling time is approximately $t^* = 104$ (more than ten vortex shedding periodicity) with a sampling frequency of 690 Hz. The data processing routine follows the same practice by Östh et al.[44] Figure 17 shows the energy fraction of the first ten POD modes of the four cases. The first modes of cases 1 and 4 without roof-jet have a dominated energy fraction, whereas the first modes of cases 2 and 3 can be hardly distinguished from the rest modes, especially for case 3 where the roof-jet plays a major role in affecting the wake. For detailed analysis, Fig. 18 plots the spatial distribution of the first POD mode with time-averaged 2D streamlines and the iso-line of $u = 0$ colored in white. The first POD modes in cases 1, 2, and 4 present qualitative similarity, namely, they are anti-symmetric about the mid-line (black dashed line). This means that the velocities in the left and right regions (behind the ship hanger)
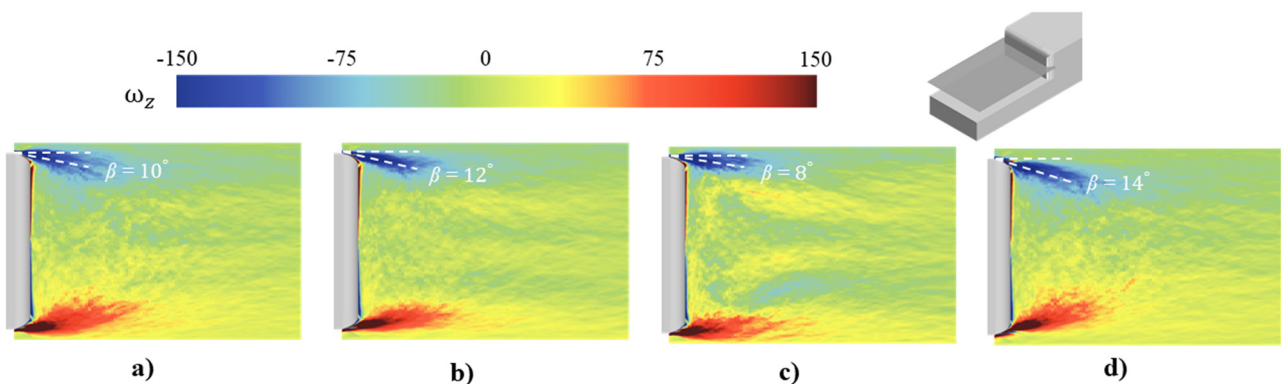


**FIG. 13.** Time-averaged z-vorticity at the z-plane: (a) case 1, (b) case 2, (c) case 3, and (d) case 4.
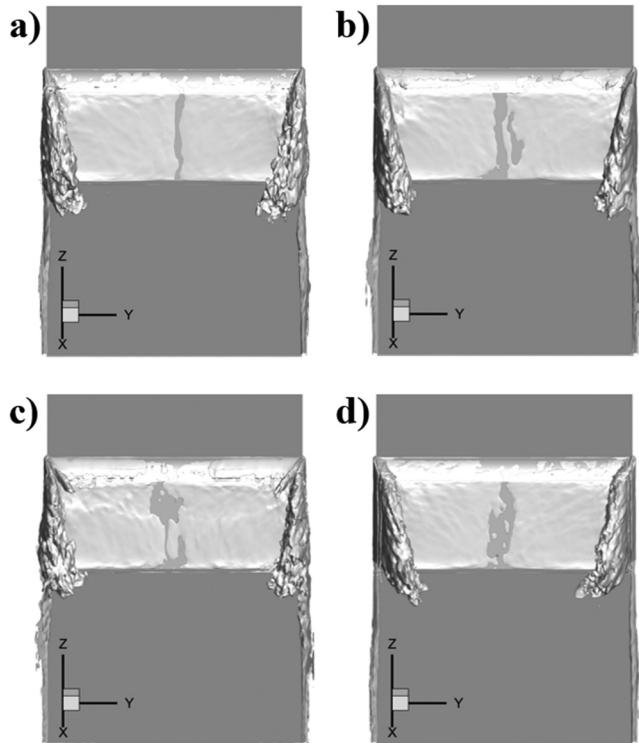
**FIG. 14.** Iso-surface of the time-averaged z-vorticity = ±90: (a) case 1, (b) case 2, (c) case 3, and (d) case 4.

are anti-correlated as the result of the asymmetric wake shifting between the left and right sides alternately. This is similar to the observation behind Ahmed bodies as reported by Aleyasin et al.,[45] Pavia et al.,[46] and Fan et al.[47] Comparatively, the first POD mode in case 3 presents a symmetric pattern. This is because the strong roof-jet applied in case 3 substantially reduces the re-circulation region as shown in Figs. 8–10. The wake is, therefore, more stable with suppressed shifting motion, and the first POD mode becomes symmetric. This explains the aforementioned difference in energy fraction observed in Fig. 17 that case 3 has no dominated first mode due to the

suppressed wake motion. The roof-jet with a reduced $C_\mu$ in case 2 is not strong enough to alter the first POD mode from asymmetric to symmetric, but it still limits the wake motion to some extent as demonstrated by the mitigated energy of its first POD mode and the reduced size of anti-correlated regions in Fig. 18(b).

It is well-recognized that the unsteady velocity fluctuation deteriorates the helicopter operating condition and significantly increases pilots' workloads.[48] The influence of the steady Coanda effect on the turbulent fluctuation in the near wake is therefore discussed here using the turbulent kinetic energy (TKE) defined as $0.5(\overline{u'u'} + \overline{v'v'} + \overline{w'w'})$. Figure 19 shows the contours of TKE together with its breakdown of the fluctuating components in the x, y, and z directions, namely, $\overline{u'u'}$, $\overline{v'v'}$, and $\overline{w'w'}$. Note that all the fluctuating quantities are normalized by the square of the free-stream velocity ($U_\infty^2$). Case 1 has the high TKE region observed along the roof and sides at station 1 and is gradually mixed in station 2 and dissipated in the downstream stations. With the roof-jet applied in cases 2 and 3, high-TKE zones near the roof and center of the deck are substantially reduced with the remaining distributed near the sides of the deck. Affected by the side-jets, case 4 has the TKE enhanced near the roof region in station 1, and the high TKE regions near the sides are constrained toward the center. The variations in TKE can be attributed to the variations in the individual turbulent component. As shown in the second row of Fig. 19, the high $\overline{u'u'}$ zone near the roof and the center region in case 1 is largely mitigated in cases 2 and 3 but is increased in case 4 toward the center region. Moreover, a similar variation is also observed in $\overline{v'v'}$ as shown in the third row of Fig. 19. A reduction in $\overline{v'v'}$ occurs in cases 2 and 3, but an increment is presented in case 4 due to the v fluctuation generated by the side-blowing jet. The $\overline{w'w'}$ components are in low magnitude among the four cases as shown in the last row of Fig. 19, except a regional high $\overline{w'w'}$ zone observed at station 1 in case 3 generated by the strong roof-jet.

Figure 20 shows the iso-surface of TKE at a high value of 0.055. The high-TKE zone observed in case 1 is significantly reduced in case 2 at the center of the deck. Particularly, case 3 has the central high-TKE region virtually eliminated. Case 4, however, behaving contrarily with cases 2 and 3, has the TKE region concentrated in the center, which manifests a regional increment.

A question of interest is why the high-TKE region is mitigated in cases 2 and 3 with roof-jet but is increased in the center in case 4 with
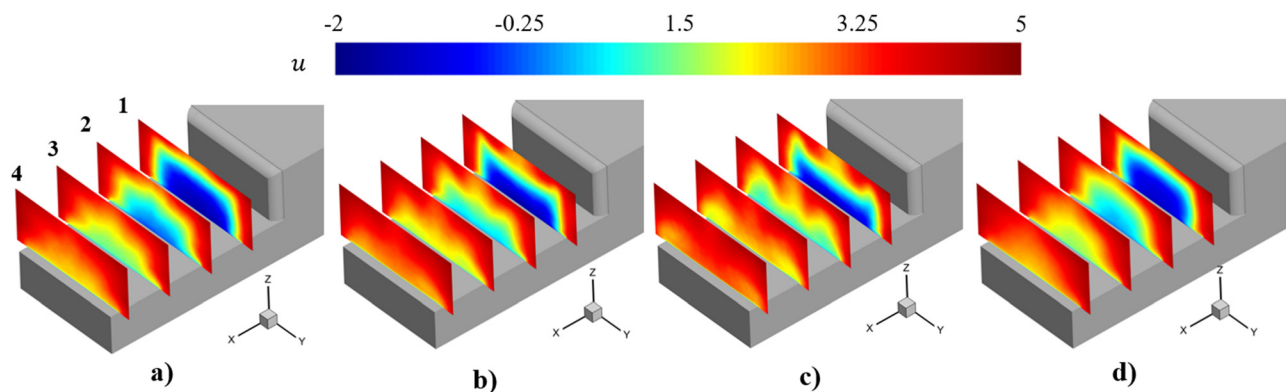


**FIG. 15.** Time-averaged u contours at different streamwise locations on the deck: (a) case 1, (b) case 2, (c) case 3, and (d) case 4.
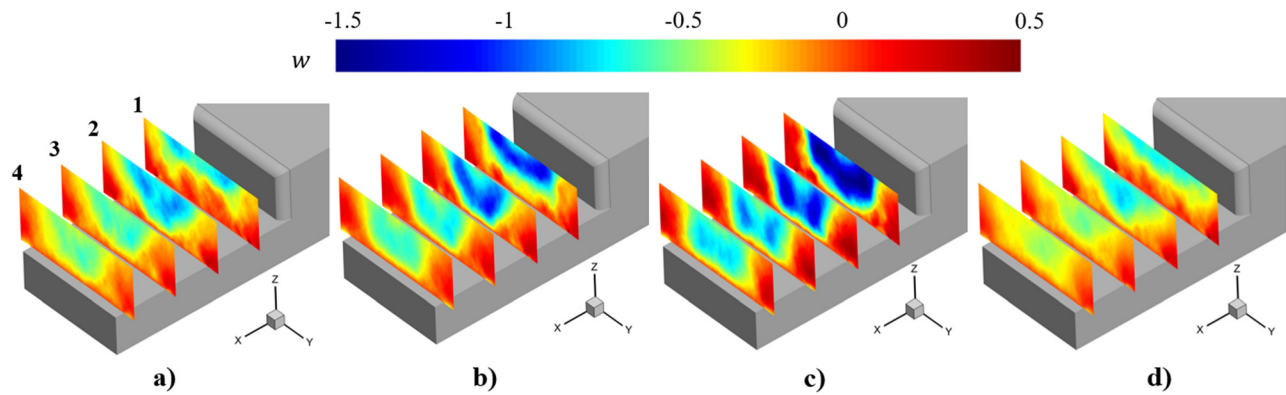
**FIG. 16.** Time-averaged $w$ contours at different streamwise locations on the deck: (a) case 1, (b) case 2, (c) case 3, and (d) case 4.

side-jets only? In fact, TKE increasing is not only observed in case 4 but also in other similar ship flow control research[9] where a steady jet is blown perpendicularly to the base along the edges. The roof-jet and side-jets introduce the variation in $u$ along the z and y directions,

respectively, which affects the shear layers characterized by Reynolds shear stresses $\overline{u'w'}$ and $\overline{u'v'}$. Therefore, explaining the variation in TKE could be approached by investigating the change of shear layers in the four cases. Figure 21 shows the iso-surfaces of high Reynolds
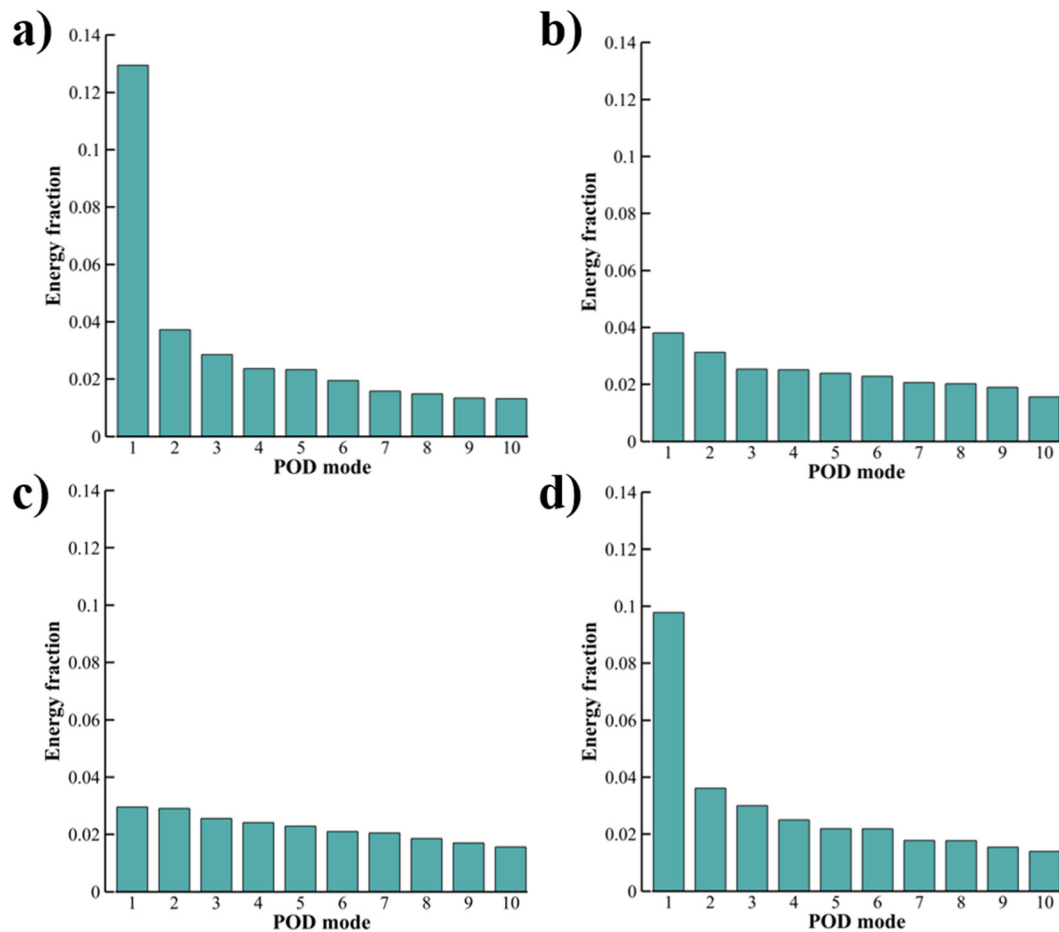


**FIG. 17.** Energy content of POD modes: (a) case 1, (b) case 2, (c) case 3, and (d) case 4.
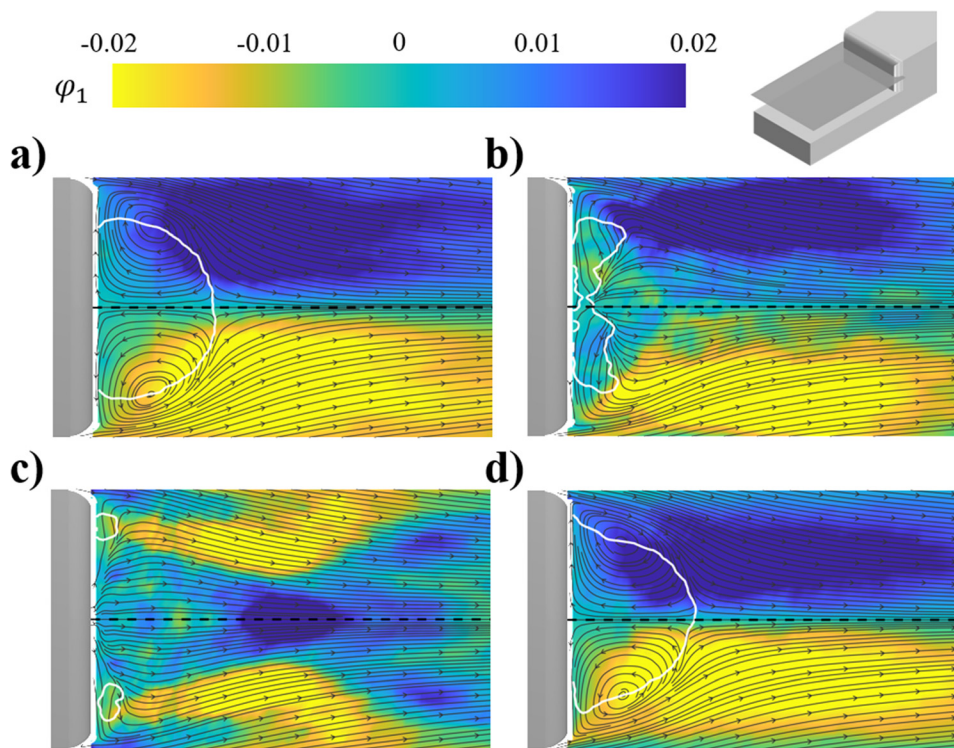
**FIG. 18.** Spatial distribution of the first POD mode: (a) case 1, (b) case 2, (c) case 3, and (d) case 4.

stresses with $\overline{u'w'} = 0.02$ (white) and $\overline{u'v'} = \pm 0.024$ (black), together with the total pressure contours at station 1. It is observed that the distributions of high shear stresses agree with those of the high TKE region in all cases. For a more detailed demonstration, Fig. 22 plots the distributions of TKE along with $\overline{u'w'}$ and $\overline{u'v'}$ at specific locations, where $\overline{u'w'}$ is extracted from station 1 and $\overline{u'v'}$ is from station 2 using the dot-dashed line shown in the top-right TKE contours. In Fig. 22(a), it can be observed that the near-roof TKE in case 3 decreases in the z-direction with the decreasing magnitude (absolute value) of $\overline{u'w'}$. Similar patterns of change can be spotted in case 4 that TKE increases with the increasing magnitude of $\overline{u'w'}$. This confirms that the variation in the shear layer causes the variations in TKE for the four cases, and the high TKE observed in case 4 near the roof is due to the high $\overline{u'w'}$. Likewise, in the y-direction Fig. 22(b), TKE follows the change of $\overline{u'v'}$ as the increase in TKE is associated with that of $\overline{u'v'}$ and vice versa. It is also shown that the high Reynolds stress $\overline{u'v'}$ region in case 1 at $y/W = -0.42 - -0.35$ is shifted to a more central region in case 4 at $y/W = -0.3 - -0.2$ due to the side-jets, which explains why TKE is concentrated toward the center region.

Then, the question becomes why the shear layer is affected differently by the roof-jet and side-jets. For the present ship model, the shear layer is a result from the mixing between the high-energy main-flow and low-energy re-circulated flow downstream the base. As shown in the total pressure contours in Fig. 21(a), the energy difference between the re-circulation region and main-flow is large, and the shear layers presented by the iso-surface are located near the boundaries between the low and high energy regions. The roof-jet attaching better on the Coanda surface as demonstrated previously (Figs. 8, 11, and 12) can effectively energize the re-circulation zone. As a result, the

energy difference between the main-flow and the re-circulation zone is alleviated, and the shear stress, especially near the roof region, is weakened as indicated in Figs. 21(b) and 21(c), which produces a lower TKE. The side-jets detaching earlier from the Coanda surface are less vectored toward the center of the deck, which fail to bring enough energy to the core re-circulation region for shear layer mitigation. Instead, the side-jets enhance the regional mixing process downstream the base by manipulating the shear layer toward the center of the deck, as evident in Figs. 21(d) and 22(b), and thus increase the central-region TKE.

This is to say, although the roof and side-jets all rely on the steady Coanda effect for flow control, their energization process is different. The roof-jet directly energizes the re-circulation zone by the momentum addition due to the vectored jet flow. In this way, the energy difference between the recirculated flow and main-flow is mitigated, which weakens the shear layer and results in lower turbulence generation. Comparatively, the energization process using side-jets is indirect that relies on shear layer manipulation to enhance mixing at the center region for energy transfer. In this way, turbulent activities are encouraged by side-jets, associated with the increase in TKE.

## V. CONCLUSIONS

The present paper studies the steady Coanda effect on the Chalmers ship model (CSM) for the ship airflow control, which investigates the control effectiveness, energization mechanism, and the influence on the flow structures on the deck. The study is conducted numerically using large eddy simulation (LES) with the wall-adapting local-eddy viscosity (WALE) model, which is validated by the experimental data acquired from the baseline CSM. To create the flow
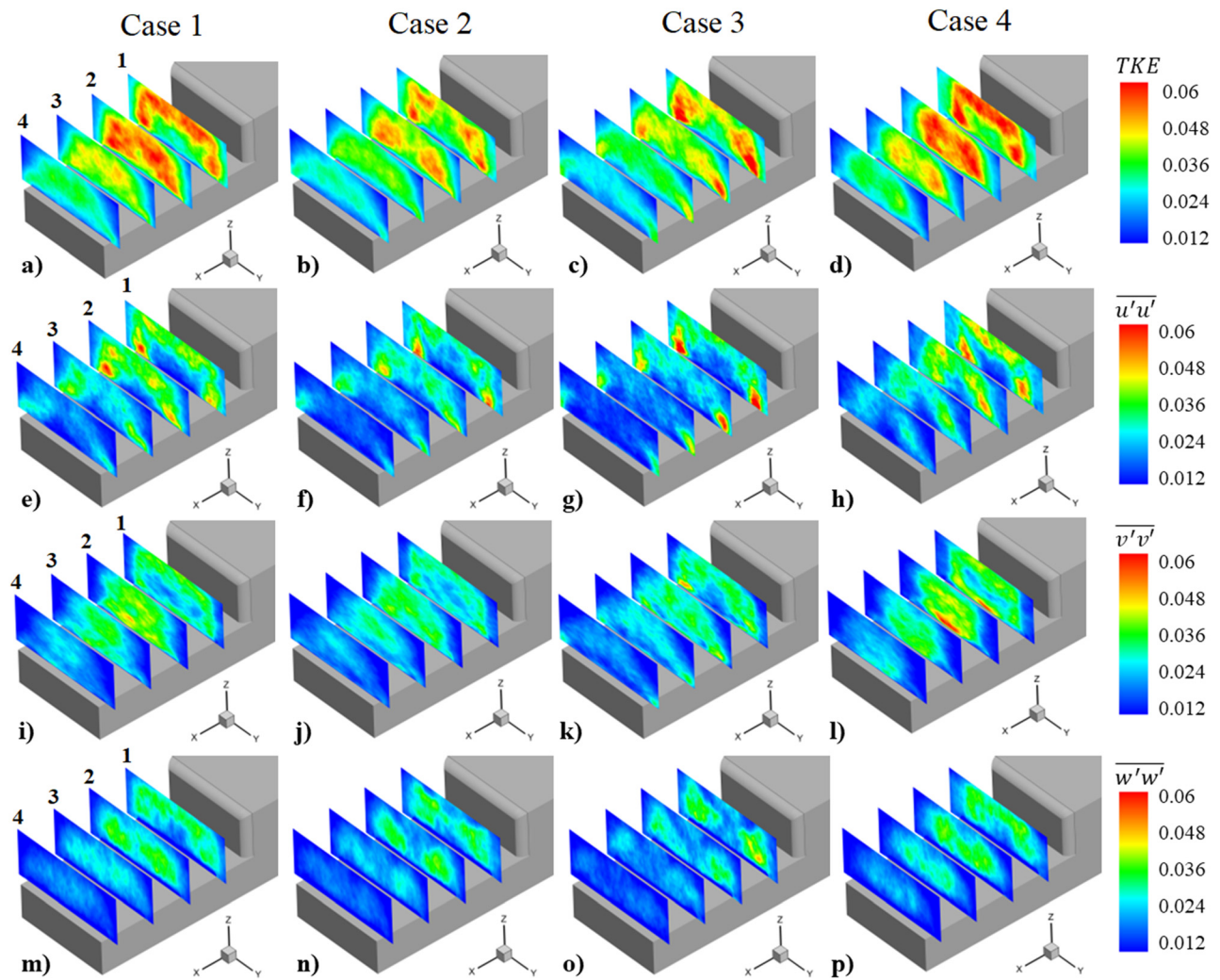
**FIG. 19.** Turbulent quantities contours at different streamwise locations on the deck: (a)–(d) turbulent kinetic energy, and (e) and (f) $\overline{u'u'}$, (i)–(l) $\overline{v'v'}$, (m)–(p) $\overline{w'w'}$.
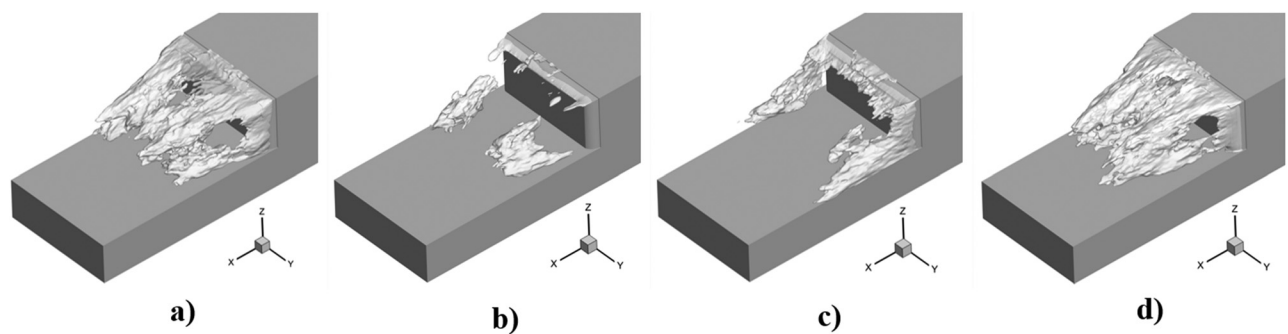


**FIG. 20.** Iso-surface of TKE = 0.055: (a) case 1, (b) case 2, (c) case 3, and (d) case 4.
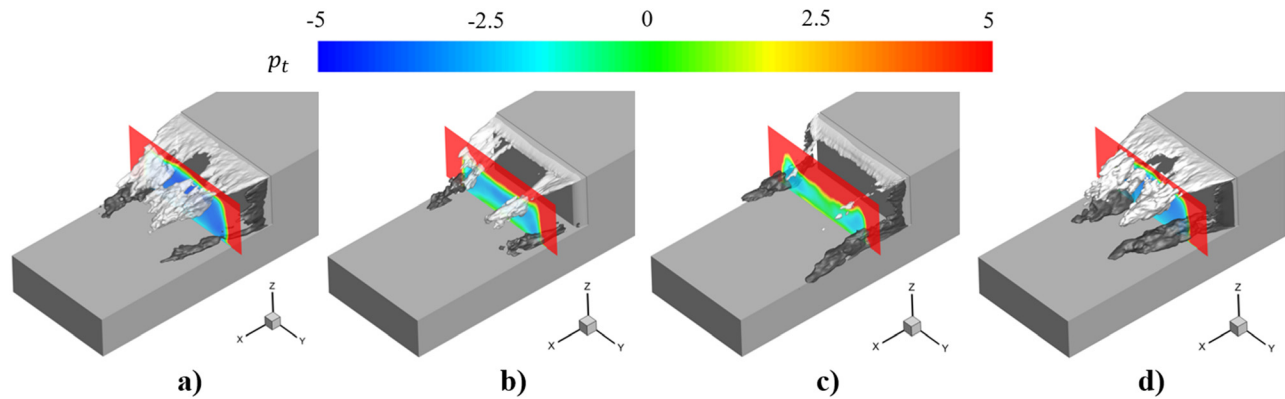
**FIG. 21.** Iso-surface of $\overline{u'w'} = 0.02$ (white), $\overline{u'v'} = \pm 0.024$ (black), and total pressure contours at station 1: (a) case 1, (b) case 2, (c) case 3, and (d) case 4.

control model, the hanger base of the baseline model is modified with the Coanda surfaces and injection slots along its roof edge and two sides edges. Four representative cases are studied: a no-jet case and three cases with the same momentum coefficient of the jet flow activated at different locations: roof, sides, and combined.

The results show that the four cases perform differently in drag reduction, vortex structures on the deck, and mean and turbulent quantities in the airwake. It is found that the roof-jet has a stronger Coanda effect and is more vectored toward the low-speed area (LSA) on the deck than the side-jets that detach earlier from the Coanda surface. The energization process is, therefore, different where the roof-jet is more effective that directly brings high momentum to LSA and side-jets manipulate the shear layer for mixing enhancement.

The roof-jet can effectively suppress the LSA on the deck, substantially reducing its height and altering the shape of the vortex core from a convex shape to concave. The airwake, as a result, is more stable as demonstrated by the POD analysis and recovers with a higher streamwise velocity and lower turbulent kinetic energy (TKE), which is of great significance to helicopter landing and takeoff. However, the down-wash flow is enhanced due to the induction effect by the roof-jet.

In contrast, the side-jets do not reduce much of the LSA but constrain the LSA toward the center of the deck. The vortex core is maintained with a convex shape but is elevated away from the deck by 8.45% compared to the no-jet case, which alleviates the down-wash effects. The TKE in the airwake is increased near the center region due to the regionally enhanced shear stresses by the side-jets.
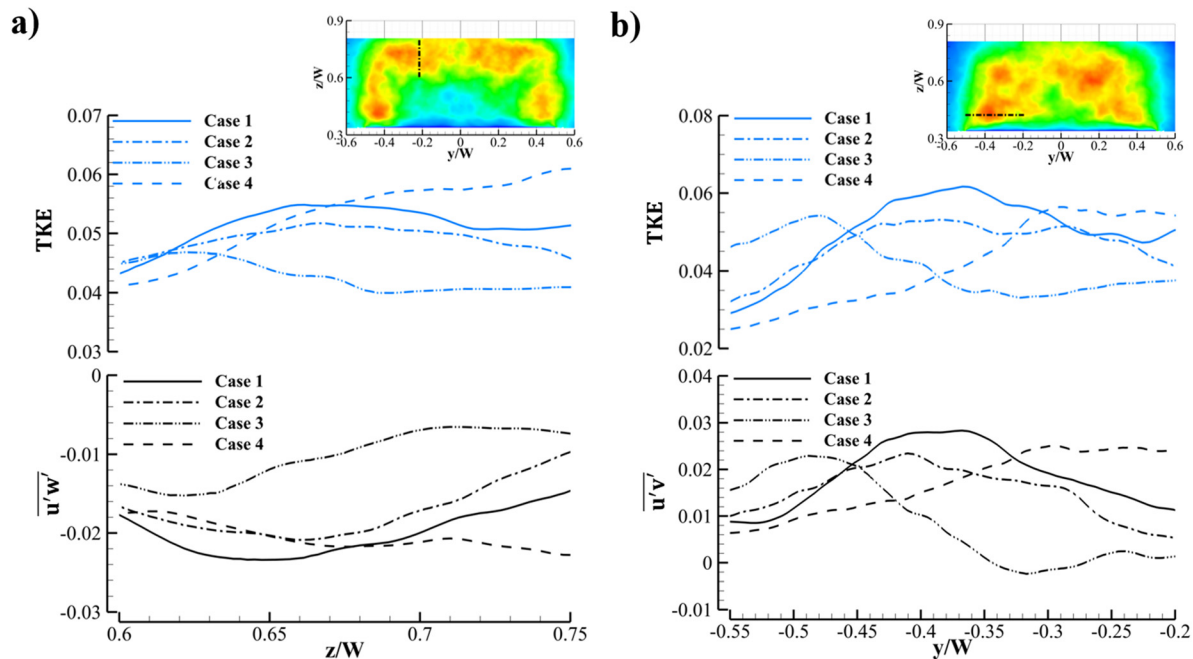


**FIG. 22.** Distributions of TKE associated with $\overline{u'w'}$ and $\overline{u'v'}$.

Combing the roof and side jets, the highest drag reduction of 7.5% is achieved due to the pressure recovery at the main base and minor offset from the pressure reduction on the roof Coanda surface.

In a nutshell, if the goal is to recover higher streamwise velocity while maintaining low TKE in the ships near wake, the roof-jet is recommended. If the goal concerns more about reducing down-wash flow at the deck region, side-jets is suggested. The combined roof-side jet will be more desirable in the case where drag reduction is the main goal.

## ACKNOWLEDGMENTS

## AUTHOR DECLARATIONS
### Conflict of Interest

The authors have no conflicts to disclose.

### Author Contributions

**Kewei Xu:** Conceptualization (equal); Data curation (equal); Formal analysis (equal); Investigation (equal); Methodology (equal); Software (equal); Validation (equal); Visualization (equal); Writing – original draft (equal); Writing – review & editing (equal). **Xinchao Su:** Investigation (supporting); Software (supporting). **Rickard Bensow:** Funding acquisition (equal); Project administration (equal); Resources (equal); Supervision (equal); Validation (equal); Writing – review & editing (equal). **Sinisa Krajnović:** Funding acquisition (equal); Project administration (equal); Supervision (equal); Validation (equal); Writing – review & editing (equal).

## DATA AVAILABILITY

The data that support the findings of this study are available from the corresponding author upon reasonable request.

## REFERENCES

[1] J. V. Healey, "The aerodynamics of ship superstructures," in Proceedings of the AGARD (1991).

[2] J. Hunt, C. Abell, J. Peterka, and H. Woo, "Kinematical studies of the flows around free or surface-mounted obstacles; applying topology to flow visualization," J. Fluid Mech. **86**, 179–200 (1978).

[3] D. M. Driver, H. L. Seegmiller, and J. G. Marvin, "Time-dependent behavior of a reattaching shear layer," AIAA J. **25**, 914–919 (1987).

[4] D. Shafer and T. Ghee, "Active and passive flow control over the flight deck of small naval vessels," AIAA Paper No. 2005-5265, 2005, p. 5265.

[5] G. Syms, "Simulation of simplified-frigate airwakes using a lattice-Boltzmann method," J. Wind Eng. Ind. Aerodyn. **96**, 1197–1206 (2008).

[6] J. S. Forrest and I. Owen, "An investigation of ship airwakes using detached-eddy simulation," Comput. Fluids **39**, 656–673 (2010).

[7] B. B. Herry, L. Keirsbulck, L. Labraga, and J.-B. Paquet, "Flow bistability downstream of three-dimensional double backward facing steps at zero-degree sideslip," J. Fluids Eng. **133**, 054501 (2011).

[8] C. H. Kääriä, Y. Wang, M. D. White, and I. Owen, "An experimental technique for evaluating the aerodynamic impact of ship superstructures on helicopter operations," Ocean Eng. **61**, 97–108 (2013).

[9] Q. Gallas, M. Lamoureux, J.-C. Monnier, A. Gilliot, C. Verbeke, and J. Delva, "Experimental flow control on a simplified ship helideck," AIAA J. **55**, 3356–3370 (2017).

[10] C. Crozon, R. Steijl, and G. Barakos, "Coupled flight dynamics and CFD–demonstration for helicopters in shipborne environment," Aeronaut. J. **122**, 42–82 (2018).

[11] W. Yuan, A. Wall, and R. Lee, "Combined numerical and experimental simulations of unsteady ship airwakes," Comput. Fluids **172**, 29–53 (2018).

[12] R. Bardera and J. Meseguer, "Flow in the near air wake of a modified frigate," Proc. Inst. Mech. Eng., Part G: J. Aerosp. Eng. **229**, 1003–1012 (2015).

[13] M. Bardera, J. C. Matías García, and A. García-Magariño, "Aerodynamic optimization over frigate helicopter flight deck by hangar shape modifications," AIAA J. **59**, 1387–1397 (2021).

[14] N. R. LaSalle, "Study of passive flow control for ship air wakes," Technical Report No. ADA581864 (Naval Academy, Annapolis, MD, 2013).

[15] C. Kaaria, "Investigating the impact of ship superstructure aerodynamics on Maritime helicopter operations," Ph.D. thesis (The University of Liverpool, 2012).

[16] S. Yongjie, H. Xiang, X. Yi, and X. Guohua, "Numerical study on flow control of ship airwake and rotor airload during helicopter shipboard landing," Chin. J. Aeronaut. **32**, 324–336 (2019).

[17] R. Bardera, J. Matías, and E. Barroso, "Experimental and numerical simulations of simple frigate with suction flow control over the deck," Ocean Eng. **236**, 109464 (2021).

[18] J. Matías-García, S. Franchini-Longhi, and R. Bardera, "Vortex generators and active flow control in the aft-deck of a frigate," in *Proceedings of the 8th European Conference for Aeronautics and Space Sciences* (EUCASS Association, Madrid, Spain, 2019), pp. 1–4.

[19] D. J. Tritton, *Physical Fluid Dynamics* (Springer Science and Business Media, 2012).

[20] S. Mohammadshahi, H. Samsam-Khayani, and K. C. Kim, "Experimental investigation on flow characteristics of compressible oscillating jet," Phys. Fluids **34**, 016111 (2022).

[21] X. Wen, Z. Li, L. Zhou, C. Yu, Z. Muhammad, Y. Liu, S. Wang, and Y. Liu, "Flow dynamics of a fluidic oscillator with internal geometry variations," Phys. Fluids **32**, 075111 (2020).

[22] N.-X. Shi, Y.-S. Gu, Y.-H. Zhou, L.-X. Wang, C. Feng, and L.-K. Li, "Mechanism of hysteresis and uncontrolled deflection in jet vectoring control based on COANDA effect," Phys. Fluids **34**, 084107 (2022).

[23] K. Xu, X. Su, R. Bensow, and S. Krajnovic, "Drag reduction of ship airflow using steady COANDA effect," Ocean Eng. **266**, 113051 (2022).

[24] J. Freund and M. Mungal, "Drag and wake modification of axisymmetric bluff bodies using COANDA blowing," J. Aircr. **31**, 572–578 (1994).

[25] D. Barros, J. Borée, B. R. Noack, A. Spohn, and T. Ruiz, "Bluff body drag manipulation using pulsed jets and COANDA effect," J. Fluid Mech. **805**, 422–459 (2016).

[26] Y. Haffner, J. Borée, A. Spohn, and T. Castelain, "Unsteady COANDA effect and drag reduction for a turbulent wake," J. Fluid Mech. **899**, A36 (2020).

[27] T. Shaqarin, P. Oswald, B. Noack, and R. Semaan, "Drag reduction of a d-shaped bluff-body using linear parameter varying control," Phys. Fluids **33**, 077108 (2021).

[28] D. Veerasamy, A. Tajik, L. Pastur, and V. Parezanović, "Effect of base blowing by a large-scale fluidic oscillator on the bistable wake behind a flat-back Ahmed body," Phys. Fluids **34**, 035115 (2022).

[29] D. Geropp and H.-J. Odenthal, "Drag reduction of motor vehicles by active flow control using the COANDA effect," Exp. Fluids **28**, 74–85 (2000).

[30] J.-D. Kee, M.-S. Kim, and B.-C. Lee, "The COANDA flow control and Newtonian concept approach to achieve drag reduction of passenger vehicle," SAE Trans. **110**, 1383–1400 (2001); available at http://www.jstor.org/stable/44730994.

[31] G. Jones, S. Viken, A. Washburn, L. Jenkins, and C. Cagle, "An active flow circulation controlled flap concept for general aviation aircraft applications," AIAA Paper No. 2002-3157, 2002, p. 3157.

[32] N. Sellars, N. Wood, and A. Kennaugh, "Delta wing circulation control using the COANDA effect," AIAA Paper No. 2002-3269, 2002, p. 3269.

[33] G. S. Jones, "Pneumatic flap performance for a 2d circulation control airfoil, steady and pulsed," Appl. Circ. Control Technol. **214**, 191–244 (2005).

[34] R. Seele, E. Graff, J. Lin, and I. Wygnanski, "Performance enhancement of a vertical tail model with sweeping jet actuators," AIAA Paper No. 2013-411, 2013, p. 411.

[35] F. Nicoud and F. Ducros, "Subgrid-scale stress modelling based on the square of the velocity gradient tensor," Flow Turbul. Combust. **62**, 183–200 (1999).

[36] D. E. Aljure, O. Lehmkuhl, I. Rodriguez, and A. Oliva, "Flow and turbulent structures around simplified car models," Comput. Fluids **96**, 122–135 (2014).

[37] L. Dalla Longa, O. Evstafyeva, and A. Morgans, "Simulations of the bi-modal wake past three-dimensional blunt bluff bodies," J. Fluid Mech. **866**, 791–809 (2019).

[38] K. He, G. Minelli, J. Wang, T. Dong, G. Gao, and S. Krajnović, "Numerical investigation of the wake bi-stability behind a notchback Ahmed body," J. Fluid Mech. **926**, A36 (2021).

[39] K. He, G. Minelli, J. Wang, G. Gao, and S. Krajnović, "Assessment of LES, IDDES and RANS approaches for prediction of wakes behind notchback road vehicles," J. Wind Eng. Ind. Aerodyn. **217**, 104737 (2021).

[40] J. Zhang, G. Minelli, A. N. Rao, B. Basara, R. Bensow, and S. Krajnović, "Comparison of PANS and LES of the flow past a generic ship," Ocean Eng. **165**, 221–236 (2018).

[41] A. N. Rao, J. Zhang, G. Minelli, B. Basara, and S. Krajnović, "Qualitative assessment of the bi-stable states in the wake of a finite-width double backward facing step," J. Wind Eng. Ind. Aerodyn. **186**, 241–249 (2019).

[42] J. Zhang, G. Minelli, B. Basara, R. Bensow, and S. Krajnović, "Yaw effect on bi-stable air-wakes of a generic ship using large eddy simulation," Ocean Eng. **219**, 108164 (2021).

[43] U. Piomelli and J. R. Chasnov, "Large-eddy simulations: Theory and applications," in *Turbulence and Transition Modelling* (Springer, 1996), pp. 269–336.

[44] J. Östh, B. R. Noack, S. Krajnović, D. Barros, and J. Borée, "On the need for a nonlinear subscale turbulence term in POD models as exemplified for a high-Reynolds-number flow over an Ahmed body," J. Fluid Mech. **747**, 518–544 (2014).

[45] S. S. Aleyasin, M. F. Tachie, and R. Balachandar, "Characteristics of flow past elongated bluff bodies with underbody gaps due to varying inflow turbulence," Phys. Fluids **33**, 125106 (2021).

[46] G. Pavia, M. Passmore, M. Varney, and G. Hodgson, "Salient three-dimensional features of the turbulent wake of a simplified square-back vehicle," J. Fluid Mech. **888**, A33 (2020).

[47] Y. Fan, C. Xia, S. Chu, Z. Yang, and O. Cadot, "Experimental and numerical analysis of the bi-stable turbulent wake of a rectangular flat-backed bluff body," Phys. Fluids **32**, 105111 (2020).

[48] R. G. Lee and S. J. Zan, "Wind tunnel testing of a helicopter fuselage and rotor in a ship airwake," J. Am. Helicopter Soc. **50**, 326–337 (2005).